Synthesis, structure and vibrational properties of GdIG$_X$:YIG$_{1-X}$ ferrimagnetic ceramic composite

P.B.A. Fechine [a,b,c,*], E.N. Silva [d], A.S. de Menezes [e], J. Derov [f], J.W. Stewart [f], A.J. Drehman [f], I.F. Vasconcelos [g], A.P. Ayala [d], L.P. Cardoso [e], A.S.B. Sombra [c]

[a] *Departamento de Química Analítica e Físico-Química, Universidade Federal do Ceará—UFC, Campus do Pici, CP 12100, CEP 60451-970 Fortaleza, CE, Brazil*
[b] *Departamento de Química Orgânica e Inorgânica—UFC, Brazil*
[c] *Laboratório de Telecomunicações e Ciência e Engenharia de Materiais (LOCEM), Departamento de Física, Universidade Federal do Ceará–UFC, Brazil*
[d] *Departamento de Física, Universidade Federal do Ceará*
[e] *IFGW, Universidade Estadual de Campinas—UNICAMP, CP 6165, 13083-970 Campinas, SP, Brazil*
[f] *Air Force Research Laboratory, Sensors Directorate, 80 Scott Drive, Hanscom AFB, MA 01731, USA*
[g] *Departmento de Engenharia Metalurgica e de Materiais, Universidade Federal do Ceara, Fortaleza, Ceara, CEP 60455-760 Brazil*

ARTICLE INFO

ABSTRACT

$Y_3Fe_5O_{12}$ (YIG) crystal has many attractive characteristics, such as low dielectric loss, narrow resonance linewidth in microwave region and also possesses a good saturated magnetization value. Composite technology in general sets out to combine materials in such a way that the properties of the composite are the optimum for a particular application. The different materials work together to give a composite of unique properties. In this work, we present the preparation procedure (obtaining) of the GdIG$_X$:YIG$_{1-X}$ ferrimagnetic ceramic matrix composite by mechanical alloying and calcinations. Besides that, we study its properties by X-ray powder diffraction, infrared, Micro-Raman, ^{57}Fe Mössbauer spectroscopy and hysteresis loop measurements.

© 2008 Elsevier Ltd. All rights reserved.

1. Introduction

Ferrimagnetic ceramics are an important kind of material used for electronic devices as tunable microwave devices (radar, telecommunication and RF measurement systems) [1], circulators [2], isolators, phase shifters, tunable filters and nonlinear devices [3]. $Y_3Fe_5O_{12}$ (YIG) is an example of ferrimagnetic ceramics widely applied in passive microwave devices. It belongs to a group of magnetic oxides, characterized by specific magnetic and magneto-optical properties. YIG crystal has many attractive characteristics, such as low dielectric loss, narrow resonance linewidth in microwave region and also possesses a good saturated magnetization value [4]. A new generation of devices [5], such as delay lines, tuning filters, oscillators, isolators and bubble-storage memory units, has been developed on a YIG basis. It is also applied in telecommunications and magneto-optic engineering.

YIG crystal structure has a cubic symmetry and belongs to the space group O_h^{10}–$Ia3d$ [6]. In a YIG structure, rare earth Y^{3+} ions occupy dodecahedral {24c} sites and tetrahedral (24d) sites. All the polyhedra in garnets are distorted and twisted. The existence of crystallographic sites of different sizes makes it possible to substitute the YIG for a wide variety of ionic radii and valence states, which leads to a range of magnetic properties. The desired properties for specific applications have been provided by controlling the preparation conditions or by the addition of appropriate substitutions to the garnet.

YIG powder can be obtained by co-precipitation [7], microwave synthesis [8], sol–gel [9] or solid-state procedure [10]. Chemical vapor deposition and vacuum sputtering were used in the preparation of thin YIG films. Its crystals can be produced by crystallization from the glass melt. Polycrystalline synthesis of bulk material is performed using classical solid state reaction methods between Y_2O_3 and Fe_2O_3 oxides at high temperature (above 1600 °C) with lengthy sintering time (several hours) [11]. Recently, Buscaglia et al. [12] synthesized YIG by sol–gel combustion process.

For large modifications of the magnetic properties of YIG materials, the doping method is usually the easiest procedure [13]. Therefore, much research on the substitution of YIG materials with respect to the magneto-optical and magnetic properties has been done [14,15]. For instance, gadolinium iron garnet ($Gd_3Fe_5O_{12}$-GdIG) is a total substitution of yttrium element for gadolinium. The importance of this substitution is the

* Corresponding author at: Departamento de Química Analítica e Físico-Química, Universidade Federal do Ceará–UFC, Campus do Pici, CP 12100, CEP 60451-970 Fortaleza,CE, Brasil. Tel.: +5585 33669980; fax: +5585 33669982.
E-mail address: fechine@ufc.br (P.B.A. Fechine).

existence of a region in the magnetization versus temperature curve [16], between the compensation point, T_{CP}, and the Curie temperature, T_C, in which the magnetization is approximately constant ($dM/dT \sim 0$), which makes the difference for some particular microwave devices [17].

Composite technology, in general, sets out to combine materials in such a way that the properties of the composite are optimum for a particular application. It can be studied as a ceramic material made from two or more phases that remain separate and distinct on a macroscopic level while forming a single component. The different materials work together to give a composite of unique properties. The resultant ceramic properties and processing requirements depend on the choice of components, relative amounts, shapes, distributions and preparations of the two or more constituents.

In this paper we present the YIG and GdIG synthesis by mechanical alloying and calcination, as well as the obtaining of the $GdIG_X{:}YIG_{1-X}$ ferrimagnetic composite. The aim of the present work is also to describe features of crystalline structure and vibrational properties of the composites by X-ray powder diffraction (XRPD), ^{57}Fe Mössbauer, Micro-Raman, infrared spectroscopy and hysteresis loop measurements.

2. Experimental methods

2.1. Ferrimagnetic sample preparation and equipments

Stoichiometric mixture of Y_2O_3 (99.99%, Aldrich) and Fe_2O_3 (99.00%, Aldrich) was used in the YIG preparation. The material was grounded on a Fritsch Pulverisette 6 planetary mill in sealed stainless-steel vials ($221.69\,cm^3$) and balls ($\varnothing$ 10 mm), under air, at weight ratio 1/9 (wt. of mixture powder/wt. of balls). Mechanical alloying was performed for 1 h of milling with 370 rpm. After this, the powder was submitted to calcination in air at 1150 °C for 5 h. The reaction occurring during calcination can be summarized as

$$3Y_2O_3 + 5Fe_2O_3 \rightarrow 2Y_3Fe_5O_{12}(YIG) \qquad (1)$$

Gd_2O_3 (99,9%, Fluka) and Fe_2O_3 (99.0%, Aldrich) powder mixture had the same treatment utilized by YIG starting materials. However, this mixture powder was submitted to calcination in air at 1250 °C for 5 h. The reaction occurring during calcination can be summarized as

$$3Gd_2O_3 + 5Fe_2O_3 \rightarrow 2Gd_3Fe_5O_{12}(GdIG) \qquad (2)$$
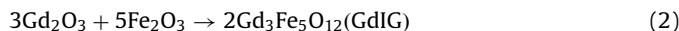
Depending on the synthesis procedure, (1) and (2) transformation results in the appearance of intermediate compounds with a perovskite structure; $YFeO_3$ and $GdFeO_3$ for YIG and GdIG, respectively:

$$Y_2O_3 + Fe_2O_3 \rightarrow 2YFeO_3(YFO) \qquad (3)$$

$$Gd_2O_3 + Fe_2O_3 \rightarrow 2GdFeO_3(GdFO) \qquad (4)$$

The composite was prepared after synthesis of the ferrimagnetic ceramics (YIG and GdIG). First, 5% of a mixture 71.82 mmol of B_2O_3 (99.0%, Aldrich) was added and 10.73 mmol of Bi_2O_3 (99.9%, Aldrich)) homogenized for 10 h of milling in the calcined powder as a sintering aid. To it 5% of the organic material (glycerin, 99.5%-O Moreira & Cia Ltd.) was also added to improve plastic features. These mixtures were uniaxially pressed into pellets at approximately 111 MPa. After that, green compacts were sintered for 12 h at 1200 °C under air. The $GdIG_X{:}YIG_{1-X}$ nomenclature was utilized to differ the composites, where X (1, 0.75, 0.5, 0.25 and 0) was given in wt%.

In order to characterize the $GdIG_X{:}YIG_{1-X}$ samples, XRPD data were collected with a Philips PW 3710 diffractometer operating at 40 kV/30 mA, using Cu Kα radiation. The diffraction patterns were obtained using Bragg–Brentano geometry in step mode with a step size of 0.02° (2θ) and with a counting time of 6 s/step. Rietveld [18] refinement was performed in the diffraction patterns using the GSAS [19] program in order to obtain phase concentrations and the full-width-at half-maximum (FWHM) of the diffraction peaks. For the profile fitting, the modified Tompson–Cox–Hastings pseudo-Voigt (TCH-pV) [20] function was used in the refinement. The crystallite size and microstrain were calculated using a model based on the Young–Desai method [21] and in a weighted size-strain broadening [22]. The refined parameters were scale factor, phase fractions, 2θ-zero point, background, cell dimensions, asymmetric factor, atomic coordinates, isotropic atom displacement (temperature) parameters, and for the FWHM, were refined the Gauss (X parameter) and Lorentz (U parameter) coefficients that are related to strain and size, while the others parameters (Y, V and W) were kept fixed at the values reached for the standard sample. The P parameter was set to zero as made by Paiva-Santos et al [23]. The Al_2O_3 standard, characterized by the Rietveld method, was used to measure the instrumental line broadening.

The photomicrograph of the $GdIG_X{:}YIG_{1-X}$ pellets were obtained on a Phillips XL-30 scanning electron microscope,
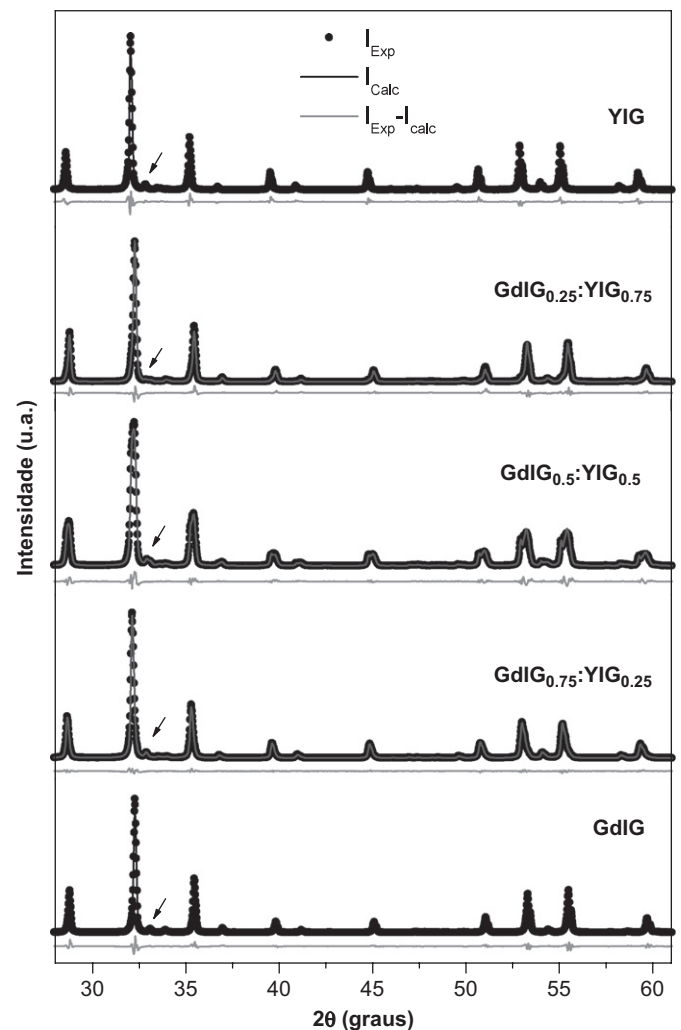

Fig. 1. Rietveld refinement of the X-ray diffraction pattern of GdIGX:YIGI-X composite powder.

operating with bunches of primary electrons ranging from 12 to 20 keV, in samples covered with a 30-nm-thick carbon layer. The microstructure of the specimens was also observed using back-scattered electrons (BSE).

The infrared spectra (FT-IR) were measured using circular pellets, made from the mixture of KBr (potassium bromate) and powder of each sample, in a ratio of KBr/sample powder near 100. This mixture was pressed with 6 ton for 15 min. All the pellets obtained present a thickness of 1.5 mm, approximately. The FT-IR were recorded in the 400–4000 cm^{-1} range with a Mattson 7000 (FT-IR) spectrometer.

Micro-Raman measurements were performed using a T64000 Jobin Yvon spectrometer equipped with an N_2-cooled charge coupled device to detect the scattered light. The spectra were excited with an argon-ion laser (4880 Å). The spectrometer slits were set to give a spectral resolution always better than 2 cm^{-1}. The Raman scattering was measured in a back-scattering geometry directly from the powder.

^{57}Fe Mössbauer spectra were taken using standard transmission geometry and a constant acceleration spectrometer, with a radioactive source of ^{57}Co in the Rh matrix. Measurements were carried out at laboratory temperature (about 294 K) on powder samples with an absorber thickness of 2 mg/cm^2. Theoretical fits using a minimum number of Lorentzian spectral components were performed with the fitting software NORMOS by R.A. Brand (distributed by Wissenschaftliche Elektronik GmbH, Germany). The spectrum consists of a set of magnetic sub-spectra related to the GdIG$_X$:YIG$_{1-X}$ structure. All the isomer shifts (δ) quoted in this paper are relative to metallic iron (α-Fe).

A Superconducting Quantum Interference Device MPMS SQUID DC Magnetometer made by Quantum Design was used to measure magnetic moment (emu) as a function of magnetic field strength. This device offers the highest accuracy for magnetic field strength measurements [24]. In its hysteresis mode, typical sensitivity of the SQUID is between 10^{-4} and 10^{-5} emu [25]. A hysteresis loop was developed using 101 data points for each sample. Measurement data were converted to Mass magnetization (emu/g) versus magnetic field strength (Oe). A field strength of 1000 Oe was sufficient to determine magnetization saturation for each sample. Calculation of the coercive field, H_C, and remanent magnetization, M_r, was enhanced by applying a piecewise cubic Hermite interpolating polynomial with 2.5 million interpolation points to the 101 measured data points. In addition, we measured the magnetization at fixed temperatures of 100, 200 and 300 K for samples.

2.2. Data analysis

2.2.1. Crystallite size and microstrain isotropic analysis

The broadening of the diffraction peaks can be attributed to the instrumental broadening, crystallite size and microstrain and the analysis and deconvolution of these peaks give information regarding the microstructure and morphology of the sample.

The mean crystallite size L_C is calculated by the Scherrer equation [26,27]

$$L_C = \frac{K\lambda}{\beta_S \cos\theta} \tag{5}$$

and the root-mean-square (r.m.s.) microstrain $\varepsilon_{r.m.s.}$, is given by [28]

$$\varepsilon_{r.m.s.} = \frac{\beta_D}{4\tan\theta} \tag{6}$$

where β_S and β_D are the integral breadths of the size-broadened (Lorentzian) and strain-broadened (Gaussian) profiles, respectively, and they are given by

$$\beta_S = \pi(X - X_{instr})/2\cos\theta \tag{7}$$

and

$$\beta_D^2 = 2\pi(U - U_{instr})\tan^2\theta \tag{8}$$

U_{instr} and X_{instr} parameters were obtained from the standard sample (Al$_2$O$_3$) refinement.

3. Results and discussion

The crystalline phases obtained from the GdIG$_X$:YIG$_{1-X}$ composite were identified by comparison of the diffractograms with the ICDD data bank. In Fig. 1 one can see the Rietveld refinement of the XRPD pattern from the GdIG$_X$:YIG$_{1-X}$ system. YIG (ICDD/PDF–70-0953) and GdIG (ICDD/PDF–74-1361) are isostructural materials with different lattice parameters. The gray lines represent the relative difference between the experimental (I_{Exp}) and the calculated (I_{Calc}) intensity obtained by the refinement. There are small fractions of antiferromagnetic phases (YFeO$_3$ and GdFeO$_3$ for YIG and GdIG, respectively) in all samples and the arrows indicate them in Fig. 1. They correspond to reactions (3) and (4), respectively. Ristic et al. [29] found the same

Table 1
Phase concentrations obtained from the Rietveld refinement of the GdIG$_X$YIG$_{1-X}$ composite.

X in wt%	Concentrations in wt%			
(GdIG$_X$:YIG$_{1-X}$)	Gd$_3$Fe$_5$O$_{12}$	Y$_3$Fe$_5$O$_{12}$	GdFeO$_3$	YFeO$_3$
1.00	97.53 (2)	–	2.47 (9)	–
0.75	76.9 (2)	20 (1)	3.10 (6)	–
0.5	36.8 (4)	59.1 (3)	2.29 (7)	1.81 (8)
0.25	20.4 (9)	77.6 (4)	0.7 (1)	1.3 (2)
0.00	–	96.18 (4)	–	3.82 (1)

Table 2
Parameters obtained from Rietveld refinement of the GdIG$_X$YIG$_{1-X}$ composite: cubic space group O_h^{10} (Ia3d). The bars separate the obtained values to each phase (GdIG/YIG).

	X = 1.00	X = 0.75	X = 0.50	X = 0.25	X = 0.00
a (Å)	12.4401(1)/–	12.4488(1)/12.3836(8)	12.4452(2)/12.3807(2)	12.4370(2)/12.3816(2)	–/12.3760(1)
V (Å^3)	1925.2/–	1929.2/1899.1	1927.55/1897.7	1923.7/1898.1	–/1895.9
φ (g/cm^3)	6.507/–	6.493/5.161	6.499/5.166	6.509/5.164	–/5.172
Fe (1)–O (Å)	2.124/–	2.020/2.161	1.993/2.049	1.894/2.156	–/2.048
Fe(2)–O (Å)	1.826/–	1.890/1.810	1.897/1.816	1.949/1.766	–/1.789
R–O (Å)	2.379/–	2.404/2.342	2.410/2.420	2.432/2.381	–/2.443
L_C (nm)	167 (14)/–	112(6)/131(16)	154 (13)/149(12)	157 (36)/148(12)	–/128(8)
$\varepsilon_{r.m.s}$ (10^{-4})	4.5 (3)/–	9.1(2)/13(2)	5.2 (4)/14(3)	24 (2)/8.3(5)	–/9.1(7)
R_{wp} (%)	11.5	5.6	7.7	11.1	11.1

The numbers (1) and (2) designate the iron atom in octahedral and tetrahedral sub-lattice, respectively.

result when they carried out the YIG synthesis by co-precipitation and calcinations. This phase was also observed when the sol–gel method is used, instead [30,31]. The mixture of all peaks from pure phases (YIG and GdIG) was observed in our samples and

Fig. 2. BSE image of GdIG$_{0.5}$:YIG$_{0.5}$ composite at an amplification of 20,000 × .

Table 3
Factor group analysis of the R$_3$Fe$_5$O$_{12}$ (R = Y and Gd) structure.

Atom	Site	Irreducible representations
Fe (1)	16a (S$_6$)	A$_{1u}$+A$_{2u}$+2E$_u$+3F$_{1u}$+3F$_{2u}$
Fe (2)	24d (S$_4$)	A$_{1u}$+A$_{2g}$+E$_g$+E$_u$+2F$_{1g}$+3F$_{1u}$+3F$_{2g}$+2F$_{2u}$
R	24c (D$^{'}$)	A$_{2g}$+A$_{2u}$+E$_g$+E$_u$+3F$_{1g}$+3F$_{1u}$+2F$_g$+2F$_{2u}$
O	96 h (C$_1$)	3A$_{1g}$+3A$_{1u}$+3A$_{2g}$+3A$_{2u}$+6E$_g$+6E$_u$+9F$_{1g}$+9F$_{1u}$+9F$_{2g}$+9F$_{2u}$

Γ_T = 3A$_{1g}$+5A$_{1u}$+5A$_{2g}$+5A$_{2u}$+8E$_g$+10E$_u$+14F$_{1g}$+18F$_{1u}$+14F$_{2g}$+16F$_{2u}$
Γ_{ac} = F$_{1u}$
Γ_s = 5A$_{1u}$+5A$_{2g}$+5A$_{2u}$ +10E$_u$+14F$_{1g}$+16F$_{2u}$
Γ_R = 3A$_{1g}$+8E$_g$+14 F$_{2g}$
Γ_{IR} = 17F$_{1u}$

Γ_T, Γ_{ac}, Γ_s, Γ_R e Γ_{IR} are the distribution of the total, acoustic, silence, Raman and infrared modes, respectively.

confirms the existence of a composite material. This characteristic was accentuated in the GdIG$_{0.5}$:YIG$_{0.5}$ sample, mainly when $2\theta > 50°$.

The identified phases and their respective concentrations, obtained by Rietveld refinement, are listed in Table 1. The corresponding crystallite size (L$_C$) and microstrain ($\varepsilon_{r.m.s.}$) results are shown in Table 2 with their respective lattice parameters. The residual error (R$_{wp}$) of the refinement was calculated and its values were acceptable. Shannon et al. [32], based in the octahedral coordination, obtained ionic radii of 1.02 and 1.06 Å for Y^{3+} and Gd^{3+}, respectively. The increase of the ionic radius also increases the lattice parameter (a) from 12.376 Å (YIG) up to 12.440 Å (GdIG). Table 2 shows the bond strength of the Fe(1)–O (octahedral site), Fe(2)–O (tetrahedral site) and R–O (dodecahedral site). The decrease of the GdIG concentration in the composites has caused changes in the lattice parameters and, consequentially, on the bond strength between ions.

Fig. 2 shows the BSE images of the GdIG$_{0.5}$:YIG$_{0.5}$ composite surface at an amplification of 20,000X. One can observe the existence of two distinct phases through the different contrasts. The GdIG grains are clearer and smaller than YIG. A reasonable homogenization can be noticed, because there is a good grain distribution between them. This could enhance the sinterization of the material and promote grain growth. Besides these features, it was identified the GdIG grains agglomerated in some places. These results collaborated to confirm the composite formation due to physical separation of the grains, when analyzed in a microscopic level.

Based on the XRDP results and using the method of site group analysis proposed by Rousseau et al. [33], the distribution of the degrees of freedom in the irreducible representations of the O$_h$ factor group was calculated (Table 3). According to this method, there are 98 vibration modes at the Brillouin zone center, but 55 (5A$_{1u}$+5A$_{2g}$+5A$_{2u}$+10E$_u$+14F$_{1g}$+16F$_{2u}$) are silent and only F$_{1u}$ is an acoustic mode. Therefore, the group theory analysis predicts 17 infrared (17F$_{1u}$) and 25 Raman (3A$_{1g}$+ 8E$_g$+14 F$_{2g}$) active modes. Table 4 shows the correlation diagram of the cations and FeO$_4$ tetrahedra into the O$_h$ point group. The 14 internal modes of the FeO4 group (2v$_1$, 4v$_2$, 4v$_3$ and 4v$_4$) are expected to be observed in the Raman spectra, whereas 7 modes (v$_2$, 3v$_3$, and 3v$_4$) should be present in FT-IR.

Table 4
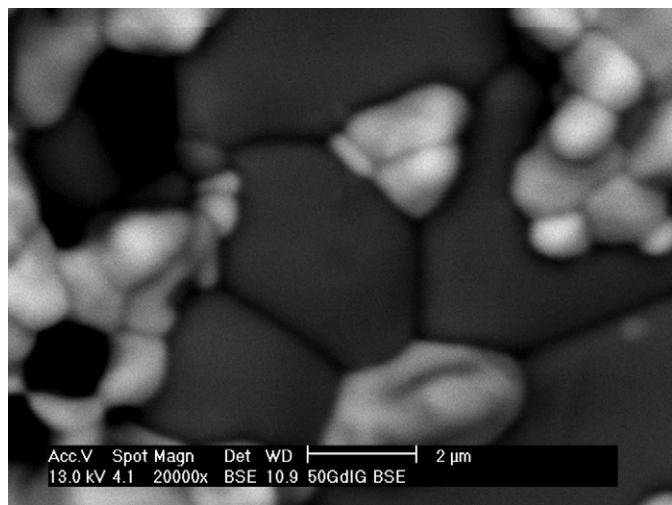Correlation table for R$_3$Fe$_2$(FeO$_4$)$_3$. The translation T$_1$, T$_2$ and T refer to Fe(1)$^{3+}$, R^{3+} and [F(2)O$_4$]$^{5-}$, respectively.

Ionic species	Free ion sym.	Site sym.	Unit cell symm.	Vibrational modes
Fe(1)-T$_1$	–	**S$_6$** A$_u^z$ E$_u^{x,y}$	**O$_h$** F$_{1u}$	17F$_{1u}$(v$_2$, 3v$_3$, 3v$_4$, 2L, 3T, 2T$_1$, 3T$_2$)
R^{3+}-T$_2$	–	**D$_2^{'}$** B$_1^z$ B$_2^y$ B$_3^x$	A$_{1g}$	3A$_{1g}$(v$_1$, v$_2$, L)
			E$_g$	8E$_g$(v$_1$, 2v$_2$, v$_3$, v$_4$, L, T, T$_2$)
[Fe(2)O$_4$]$^{5-}$	**T$_d$** (v$_1$)A$_1$ (v$_2$)E (R)F$_1$ (T,v$_3$,v$_4$)F$_2$	**S$_4$** A B E	F$_{2g}$	14F$_{2g}$(v$_2$, 3v$_3$, 3v$_4$, 2L, 3T, 2T$_2$)

The rotational (R) degree of freedom of the free molecule becomes librational (L) lattice mode in the crystal.

Fig. 3 shows the FT-IR from the $GdIG_X:YIG_{1-X}$ composite together with the pure phases. The bands from GdIG were located at 553, 595 and 645 cm^{-1}, whereas for YIG the same bands appeared at 565, 610 and 664 cm^{-1}. These three bands are associated with the asymmetric stretching (v_3) of the tetrahedron (Fe–O bond), as predicted by factor group analysis. McDevit [34] concluded that these bands had a linear behavior with ionic radius of the rare earth element. Thus, its positions decrease with increase of the unit cell [35], and consequently, the enlargement of the Fe(2)–O bond (Table 2). Our results agree with the observation of Hofmeister and Campbell [35], who observed all the infrared active phonons, through far and mid infrared measurements recorded from 700 to 100 cm^{-1}.

Raman spectra of the $GdIG_X:YIG_{1-X}$ composite are presented in Fig. 4. Through these results, one can notice four collections of modes: three between 650 and 750 cm^{-1}, two from 550 to 650 cm^{-1}, four between 390 and 550 cm^{-1} and three from 300 to 390 cm^{-1}. All these modes are associated with internal vibrations of the FeO_4 molecular group, whereas the modes under 300 cm^{-1} were labeled as translations (T) of R^{3+}, $[FeO_4]^{5-}$ and/or $[FeO_6]^{9-}$. The sequence of the internal vibrational modes observed over 300 cm^{-1} was $v_4 < v_2 < v_3 < v_1$. The splitting or the degenerated modes of the free tetrahedron have its origin in the characteristic

distortion and twisting exhibited by this group in garnets [6]. Assignments of all the observed Raman modes are described in Table 5, where a very good agreement with the predicted number of active phonons is verified.

As a rule, Raman and FT-IR of $GdIG_X:YIG_{1-X}$ compounds can be interpreted as linear combination of the corresponding spectra of the pure former compounds. This effect is clearly evidenced by observing that there is no dependence of the phonon wavenumber on sample concentration. In this way, vibrational spectroscopy provides further support to the formation of a composite instead of a solid solution.

[57]Fe Mössbauer spectroscopy was used in order to obtain information about the occupied iron sites. Fig. 5 shows the measured spectra (dots) with their respective fits (thick solid curves). The same fitting model with two overlapping sextets was used: one sextet (continuous curve) accounts for Fe^{3+} ions at sites with octahedral symmetry [16a], whereas the other one (dot straight) corresponds to Fe^{3+} at tetrahedral coordinated sites (24d). The hyperfine parameters and relative site populations obtained from the fits to the experimental data are listed in Table 6. The small amount of antiferromagnetic phases identified by XRD was not readily identifiable by Mössbauer spectroscopy due to the fact that these phases also had a sextet, with hyperfine
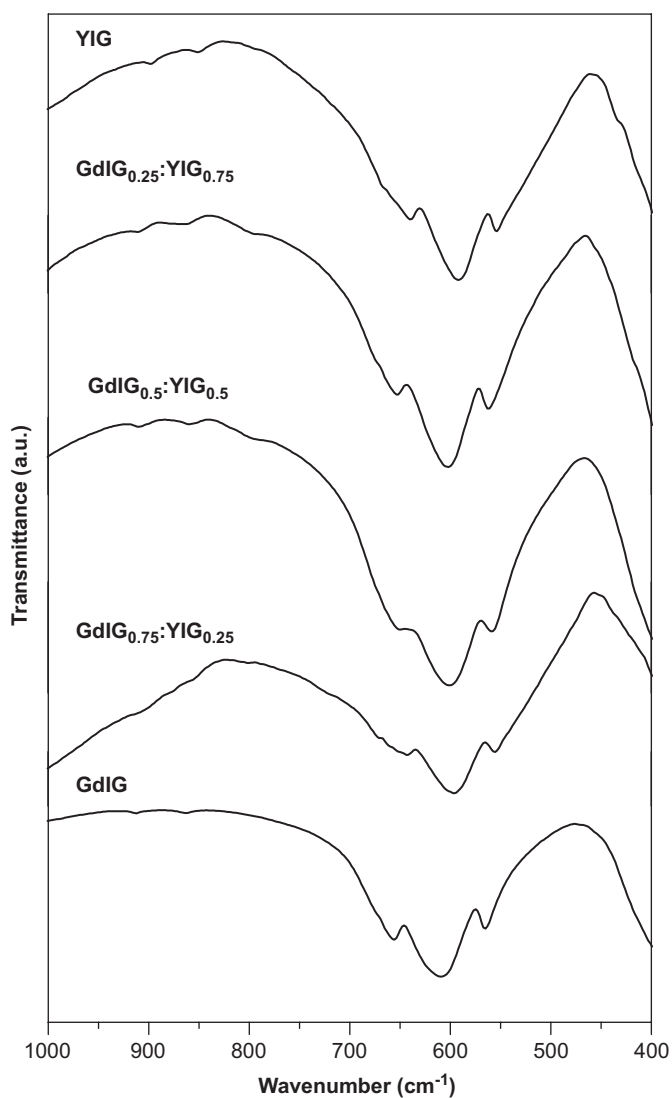

Fig. 3. Infrared spectra of $GdIG_X:YIG_{1-X}$ composites showing the v_3 internal modes of the FeO_4 group.
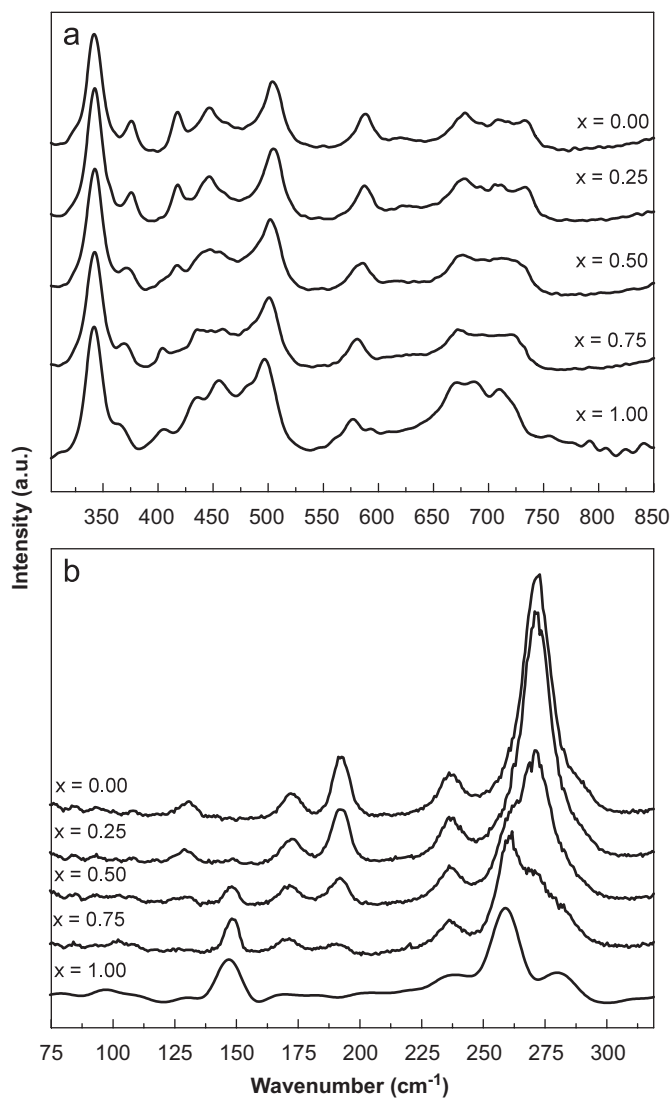

Fig. 4. Raman spectra of internal (a) and external (b) vibrational modes of the $GdIG_X:YIG_{1-X}$ system.

Table 5
Raman shift (in cm^{-1}) of $GdIG_X$:YIG_{1-X} composite.

	$X = 0.00$	$X = 0.25$	$X = 0.50$	$X = 0.75$	$X = 1.00$	Assignments
1	–	99	99	99	99	$T+T_1+T_2$
2	130	130	130	130	–	$T+T_1+T_2$
3	–	147	147	147	147	$T+T_1+T_2$
4	–	168	168	168	168	$T+T_1+T_2$
5	172	172	172	172	–	$T+T_1+T_2$
6	192	192	192	190	–	$T+T_1+T_2$
7	237	237	237	237	237	$L[FeO_4]^{5-}$
8	–	259	259	259	259	$L[FeO_4]^{5-}$
9	272	272	272	272	–	$L[FeO_4]^{5-}$
10	–	280	280	280	280	$L[FeO_4]^{5-}$
11	289	289	289	289	–	$L[FeO_4]^{5-}$
12	308	308	308	308	–	$L[FeO_4]^{5-}$
13	321	321	321	321	310	$v_4(E_g)$
14	342	342	342	342	342	$v_4(F_{2g})$
15	–	370	370	370	370	$v_4(F_{2g})$
16	376	376	376	376	–	$v_4(F_{2g})$
17	–	–	404	404	404	$v_2(E_g)$
18	418	418	418	–	–	$v_2(E_g)$
19	–	433	433	433	433	$v_2(E_g)$
20	445	445	445	445	–	$v_2(E_g)$
21	–	456	456	456	456	$v_2(F_{2g})$
22	467	467	467	467	–	$v_2(F_{2g})$
23	–	496	496	496	496	$v_2(A_{1g})$
24	504	504	504	504	–	$v_2(A_{1g})$
25	–	576	576	576	576	$v_3(F_{2g})$
26	587	587	587	587	–	$v_3(F_{2g})$
27	622	622	622	622	–	$v_3(E_g)$
28	–	671	671	671	671	$v_3(F_{2g})$
29	677	677	677	677	–	$v_3(F_{2g})$
30	–	685	685	685	685	$v_1(E_g)$
31	712	712	712	712	712	$v_1(E_g)$
32	735	733	733	733	–	$v_1(A_{1g})$

parameters similar to [16a] site from garnet [36]. As the concentration of these phases is small when compared to garnets, their sub-spectra were omitted.

Bond strength of Fe–O in the tetrahedral system is smaller than the octahedral of the garnets, see Table 2. The increased covalence increases the 4s electron density at the iron nucleus and consequently decreases the B_{HF} and δ, as demonstrated by Vandormael et al. [37]. The B_{HF} and δ values for the d and a sites, plotted as a function of GdIG weight (%) in the composite, are shown in Fig. 6. One can observe that B_{HF} and δ are higher for the octahedral site [16a] than for the tetrahedral site (24d). Both values exhibit an approximately linear dependence on the GdIG concentration. Gibb [38] explained that there is evidence of an inductive effect from the bonds to adjacent atoms and the well-known decrease in shift on reducing the coordination from six to four is more the result of the removal of the center of symmetry, which allows increased covalence with the 4p orbital, rather than the decrease in the bond distances.

Magnetic characteristics of the composites were also studied by the hysteresis loop (variation in magnetization, M, with bias field, H) as a function of the temperature, as shown in Fig. 7. This study was not realized in the $GdIG_{0.50}$:$YIG_{0.50}$ sample, due to its result being similar to the others. The individual phases (GdIG and YIG) had an additional temperature at 200 K. All the samples were studied below Curie temperature (T_C), 553 K (YIG) and 564 K (GdIG). The shape of hysteresis loop was attributed to soft ferrites due their values (Table 7) of coercive field (H_C), remanent (M_r) and saturation (M_S) magnetization. These two last values decreased as temperature increased. This effect can be understood by noting that the vibrational energy (thermal vibrations) of an atom increases with temperature, making it more difficult to align the magnetic dipoles [39]. Chen et al. [4] obtained hysteresis loop to YIG, similar to the one present in this study.
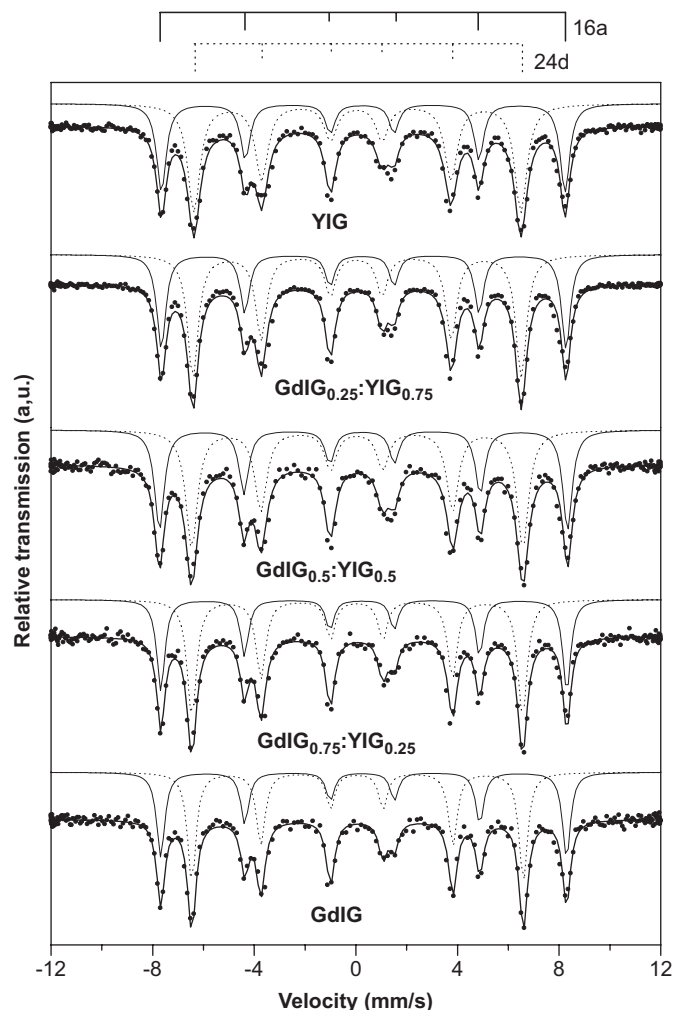
Fig. 5. Mössbauer spectra of the $GdIG_X$:YIG_{1-X} composite.

Table 6
Hyperfine parameters of the $GdIG_X$:YIG_{1-X} composites.

Sample	Sites	Hyperfines parameters			P (%)
		δ (mm/s)	Δ (mm/s)	B_{HF} (T)	
YIG	24d	0.149 (1)	0.043 (2)	39.91 (1)	62
	16a	0.377 (1)	0.041 (3)	49.25 (1)	38
$GdIG_{0.25}YIG_{0.75}$	24d	0.140 (1)	0.033 (1)	40.09 (1)	61
	16a	0.383 (1)	0.064 (1)	49.39 (1)	39
$GdIG_{0.50}YIG_{0.50}$	24d	0.153 (1)	0.021 (1)	40.42 (1)	59
	16a	0.381 (1)	0.055 (2)	49.81 (1)	41
$GdIG_{0.75}YIG_{0.25}$	24d	0.151 (1)	0.020 (2)	40.37 (1)	60
	16a	0.385 (1)	0.072 (3)	49.54 (1)	40
GdIG	24d	0.161 (1)	0.029 (2)	40.48 (1)	58
	16a	0.387 (1)	0.053 (2)	49.52 (2)	42

Parameters: δ (isomer shifts); Δ (quadrupole splitting); B_{HF} (magnetic hyperfine field); P (iron ratio percentage error ~3%).

Magnetization in garnets presents remarkable features associated with interactions between several magnetic sub-lattices, such as compensation temperature and T_C virtually independent
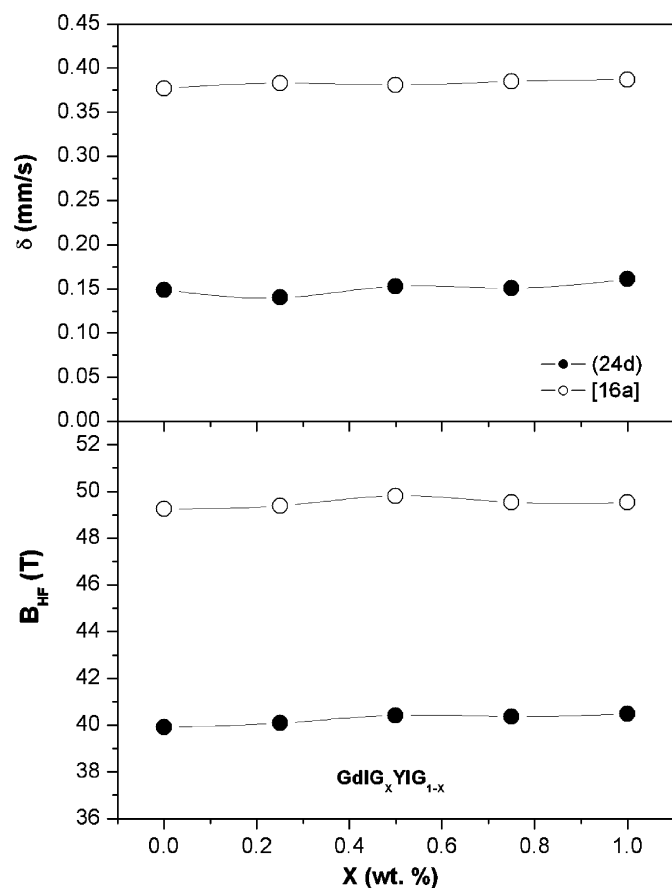
Fig. 6. Hyperfine parameter for (24d) and [16a] sites of the GdIG$_X$:YIG$_{1-X}$ composites as a function of the GdIG wt%.

of the rare-earth cation (Y^{3+} or Gd^{3+}). However, the temperature effect for M$_S$ in GdIG was greater than in YIG due to the diamagnetism of yttrium [6]. Thus, only iron sub-lattices contributed to the total magnetization in the YIG sample and this ferrite has no compensation temperature. GdIG presented similar YIG behavior at 100 K, when the compensation temperature had no influence. The behavior of GdIG$_{0.75}$:YIG$_{0.25}$ and GdIG$_{0.25}$:YIG$_{0.75}$ composites was a mixture of characteristics of the individual phases.

4. Conclusions

The GdIG$_X$:YIG$_{1-X}$ composites were satisfactorily obtained by mechanical alloying and calcination. The main features of their structure were studied by XRPD. Decreasing of the GdIG concentration in the composites caused changes in the lattice parameters. Raman and infrared bands were successfully assigned to the active phonons expected in a garnet lattice. The vibrational modes distribution, together with the negligible wavenumber dependence on the GdIG concentration, was consistent with the formation of a composite instead of a solid solution. ^{57}Fe Mössbauer spectroscopy was important to obtain information about the occupied iron sites. Iron from octahedral and tetrahedral sites was observed as two individual sub-spectra and their hyperfine parameter helped to interpret the crystalline structure. The hysteresis loop profile was attributed to soft ferrites due to their values of coercive field, remanent and saturation magnetization. These results helped one to understand the magnetic behavior of these composites as a function of the magnetic field applied and temperature of experimental calcinations.
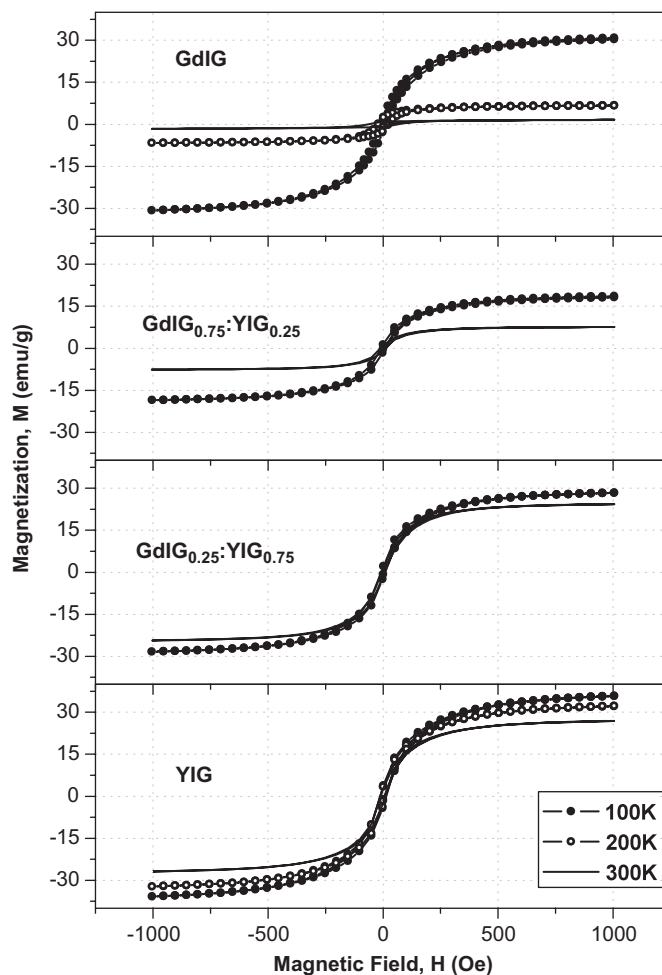

Fig. 7. SQUID measurement of magnetization, M, by mass (emu/g) as a function of magnetic field strength, H (Oe), of the GdIG$_X$:YIG$_{1-X}$ composites at 100, 200 and 300 K.

Table 7
Magnetic properties of the GdIG$_X$:YIG$_{1-X}$ composites from hysteresis loop.

	GdIG (44 mg)	GdIG$_{0.75}$YIG$_{0.25}$ (54 mg)	GdIG$_{0.25}$YIG$_{0.75}$ (23 mg)	YIG (30 mg)
100 K				
H$_C$ (Oe)	−8.8	−7.9	−8.5	−13.1
M$_r$ (emu/g)	2.2	1.1	1.8	3.5
M$_S$ (emu/g)	30.4	18.2	28.3	35.8
200 K				
H$_C$ (Oe)	−22.7	-	-	−12.1
M$_r$ (emu/g)	2.3	-	-	3.2
M$_S$ (emu/g)	6.7	-	-	32.2
300 K				
H$_C$ (Oe)	−65.3	−11.7	−5.6	−10.4
M$_r$ (emu/g)	0.9	1.0	1.2	2.5
M$_S$ (emu/g)	1.6	7.6	24.4	26.9

References

[1] A.B. Ustinov, V.S. Tiberkevich, G. Srinivasan, A.N. Slavin, A.A. Semenov, S.F. Karmanenko, B.A. Kalinikos, J.V. Mantese, R. Ramer, J. Appl. Phys. 100 (2006) 093905–093907.
[2] J.P. Ganne, R. Lebourgeois, M. Paté, D. Dubreuil, L. Pinier, H. Pascard, J. Eur. Ceram. Soc. 27 (2007) 2771.
[3] J.D. Adam, L.E. Davis, G.F. Dionne, E.F. Schloemann, S.N. Stitzer, IEEE Trans. Microwave Theory Tech. 50 (2002) 721.
[4] Y.F. Chen, K.T. Wu, Y.D. Yao, C.H. Peng, K.L. You, W.S. Tse, Microelectron. Eng. 81 (2005) 329.
[5] M. Huang, S. Zhang, Mater. Chem. Phys. 73 (2002) 314.
[6] R. Valenzuela, Magnetic Ceramics, Cambridge University Press, New York, 1994.
[7] Y.S. Ahn, M.H. Han, C.O. Kim, J. Mater. Sci. 31 (1996) 4233.
[8] T. Kimura, H. Takizawa, K. Uheda, T. Endo, M. Shimada, J. Am. Ceram. Soc. 81 (1998) 2961.
[9] R.D. Sánchez, C.A. Ramos, J. Rivas, P. Vaqueiro, M.A. López-Quintela, Phys. B 354 (2004) 104.
[10] V. Buscaglia, F. Caracciolo, C. Bottino, M. Leoni, P. Nanni, Acta Mater. 45 (3) (1997) 1213.
[11] L.B. Kong, J. Ma, H. Huang, Mater. Lett. 56 (2002) 344.
[12] X.Z. Guo, B.G. Ravi, P.S. Devi, J.C. Hanson, J. Morgolies, R.J. Gambino, J.B. Parise, S. Sampath, J. Magn. Magn. Mater. 295 (2005) 145.
[13] T.-C. Mao, J.-C. Chen, J. Magn. Magn. Mater. 302 (2006) 74.
[14] K. Shinagawa, E. Tobita, T. Saito, T. Tsushima, J. Magn. Magn. Mater. 251 (1998) 177.
[15] C.-Y. Tsay, C.-Y. Liu, K.-S. Liu, I.-N. Lin, L.-J. Hu, T.-S. Yeh, J. Magn. Magn. Mater. 239 (2002) 490.
[16] S.C. Zanatta, L.F. Cótica, A. Paesano Jr., S.N. de Medeiros, J.B.M. da Cunha, B. Hallouche, J. Am. Ceram. Soc. 88 (2005) 3316.
[17] A.S. Hudson, J. Phys. D: Appl. Phys. 3 (1970) 251.
[18] H.M. Rietveld, J. Appl. Crystallogr. 10 (1969) 65.
[19] A.C. Larson, R.B. Von Dreele, General Structure Analysis System (GSAS), Los Alamos National Laboratory Report LAUR, 86-748, 2004.
[20] P. Tompson, D.E. Cox, J.B. Hastings, J. Appl. Crystallogr. 20 (1987) 79.
[21] R.A. Young, P. Desai, Arch. Nauki. Mater. 10 (1989) 71.
[22] C.O. Paiva-Santos, H. Gouveia, W.C. Lãsa, J.A. Varela, Mater. Struct. 6 (2) (1999) 111.
[23] C.O. Paiva-Santos, A.A. Cavalheiro, M.A. Zaghete, M. Cilense, J.A. Varela, M.T. Silva Giotto, Y.P. Mascarenhas, Adv. X-ray Anal. 44 (2001) 38.
[24] J.G. Webster (Ed.), The Measurement, Instrumentation, and Sensors Handbook, CRC Press, Boca Raton, FL, 1999.
[25] Quantum Design, San Diego, CA, Magnetic Property Measurement System Software User's Manual, 1996.
[26] P. Scherrer, Nachr. Ges. Wiss. Gottingen, Math.-Phys. Kl. 2 (1918) 96.
[27] L.V. Azároff, Elements of X-ray Crystallography, McGraw-Hill, New York, 1968.
[28] A.R. Stokes, A.J.C. Wilson, Proc. Phys. Soc. Lond. 56 (1944) 174.
[29] M. Ristic', I. Nowik, S. Popovic', I. Felner, S. Music', Mater. Lett. 57 (2003) 2584.
[30] P. Vaqueiro, M.P. Crosnier-Lopez, M.A. López-Quintela, J. Solid State Chem. 126 (1996) 161.
[31] J.S. Kum, S.J. Kim, In-Bo Shim, C.S. Chul Sung Kim, J. Magn. Magn. Mater. 272 (2004) 2227.
[32] R.D. Shannon, C.T. Prewitt, Acta Crystallogr. B 25 (1969) 925.
[33] D.L. Rousseau, R.P. Bauman, S.P.S. Porto, J. Raman Spectrosc. 253 (1981) 10.
[34] N.T.J. McDevitt, Opt. Soc. Am. 834 (1967) 57.
[35] A.M. Hofmeister, K.R. Campbell, J. Appl. Phys. 72 (1992) 638.
[36] S. Mathur, M. Veith, R. Rapalaviciute, H. Shen, G.F. Goya, W.L. Martins, T.S. Berquo, Chem. Mater. 1906 (2004) 16.
[37] D. Vandormael, F. Grandjean, D. Hautot, G.J. Long, J. Phys.: Condens. Matter 13 (2001) 1759.
[38] T.C. Gibb, in: Mössbauer Spectroscopy. V. 5. Encyclopedia of Inorganic Chemistry, Wiley, Chichester, 1994.
[39] D.M. Pozar, Microwave Engineering, second ed., Wiley, Inc., New York, 1998.